
Multi-Cohort Development and Validation of 2D and 3D Deep Learning Models for MRI-based Parkinson’s Disease Classification: A Comparative Analysis of Convolutional Kolmogorov-Arnold Networks, Convolutional Neural Networks, and Graph Convolutional Networks

SB Patel

Nuffield Department of Clinical Neuroscience
University of Oxford
salil.patel@endcn.ox.ac.uk

V Goh

School of Biomedical Engineering and Imaging Sciences
King's College London
vicky.goh@kcl.ac.uk

JJ FitzGerald

Nuffield Department of Surgery
University of Oxford
james.fitzgerald@nds.ox.ac.uk

CA Antoniades

Nuffield Department of Clinical Neuroscience
University of Oxford
chrystalina.antoniades@endcn.ox.ac.uk

ABSTRACT

Early and accurate diagnosis of Parkinson’s Disease (PD) remains challenging. This study compares deep learning architectures for MRI-based PD classification, introducing the first three-dimensional (3D) implementation of Convolutional Kolmogorov-Arnold Networks (ConvKANs), a new approach that combines convolution layers with adaptive, spline-based activations, offering enhanced flexibility in modelling complex, non-linear relationships.

We evaluated Convolutional Neural Networks (CNNs), ConvKANs, and Graph Convolutional Networks (GCNs) using three open-source datasets; a total of 142 participants (75 with PD and 67 age-matched healthy controls). For 2D analysis, we extracted 100 axial slices centred on the midbrain from each T1-weighted scan. For 3D analysis, we used the entire volumetric scans. ConvKANs integrate learnable B-spline functions with convolutional layers. GCNs represent MRI data as graphs, theoretically capturing structural relationships that may be overlooked by traditional approaches. Interpretability visualizations, including the first ConvKAN spline activation maps, and projections of graph node embeddings, were depicted.

ConvKANs demonstrated high performance across datasets and dimensionalities, achieving the highest 2D AUROC (0.98) in one dataset and matching CNN peak 3D performance (1.00). CNN models performed well, while GCN models improved in 3D analyses, reaching up to 0.97 AUROC. 3D implementations yielded higher AUROC values compared to 2D counterparts across all models.

ConvKAN implementation shows promise for MRI analysis in PD classification, particularly in the context of early diagnosis. The improvement in 3D analyses highlights the value of volumetric data in capturing subtle PD-related changes. While MRI is not currently used for PD diagnosis, these findings suggest its potential as a component of a multimodal diagnostic approach, especially for early detection. Future research should focus on larger-scale validation, integration with other modalities, and further exploration of 3D ConvKANs for early PD diagnosis.

Introduction

Parkinson's Disease (PD) is a progressive neurodegenerative disorder characterized by motor symptoms such as tremor, rigidity, and bradykinesia, as well as non-motor symptoms including cognitive impairment and depression.¹ Early and accurate diagnosis of PD remains challenging, with current methods relying heavily on subjective, clinical assessment.²

Magnetic Resonance Imaging (MRI) is a non-invasive imaging technique that employs magnetic fields and radio waves to generate detailed images of the body's internal structures.³ MRI scans provide excellent soft tissue contrast and are used by clinicians to diagnose a multitude of neurological pathologies including tumours, strokes and multiple sclerosis.

However, the subtle and heterogeneous brain changes in PD are not often noted on MRI scans, and imaging is not part of standard PD diagnostic criteria.⁴

Deep learning, a subset of machine learning inspired by the multi-layered nature of biological neural networks, has been applied successfully to image analysis tasks across various domains, including medical imaging.^{5,6} The application of deep learning to MRI analysis has the potential to enhance our understanding of neurological disorders and improve patient outcomes. However, the optimal approach for using deep learning in MRI analysis remains an open question.

Traditional Convolutional Neural Networks (CNNs) have been widely used in medical image analysis.⁷ These networks excel at capturing hierarchical features through successive layers of convolution and pooling operations. However, the rigid structure of CNNs may limit their ability to capture complex, non-linear relationships in high-dimensional medical imaging data. In response to these limitations, novel architectures have emerged. The Kolmogorov-Arnold Network (KAN), introduced earlier this year, represents a significant departure from traditional CNN architectures.⁸ Based on the Kolmogorov-Arnold representation theorem, KANs replace conventional weight matrices with learnable spline functions, offering enhanced flexibility in modelling complex, non-linear relationships.

Building upon the KAN framework, the Convolutional Kolmogorov-Arnold Network (ConvKAN) was recently proposed as a fusion of KAN principles with convolutional architectures.⁹ ConvKANs integrate spline-based activation functions directly into convolutional layers, offering the best of both worlds: the spatial invariance properties of CNNs and the flexible, non-linear modelling capabilities of KANs. While ConvKANs have shown promising results in 2D image analysis tasks, their application to 3D imaging data, such as volumetric MRI scans, represents a novel and unexplored step.¹⁰

Graph-based approaches have gained traction in the deep imaging community and graph Convolutional Networks (GCNs) offer a framework for modelling the inherent structural relationships in medical imaging data including in PD.¹¹ By representing an image or scan as a graph of interconnected nodes, GCNs can capture both local and global context, overcoming limitations of traditional CNN architectures.¹² In the context of MRI analysis, graph-based approaches allow for the incorporation of anatomical knowledge and the modelling of long-range dependencies that may be crucial for accurate diagnosis and prognosis.¹³

The dimensionality of input data represents another critical consideration in MRI analysis. Traditional approaches often rely on 2D slice-based analysis, where volumetric MRI scans are treated as a series of independent 2D images. This approach, while computationally efficient, may fail to capture important 3D spatial relationships within the brain. Conversely, full 3D analysis considers the entire volumetric data, extracting more features at the cost of increased computational complexity.

The trade-offs between 2D and 3D approaches extend beyond mere computational considerations. 2D slice-based methods benefit from larger datasets, as each MRI volume yields multiple training samples. However, these methods may struggle to capture long-range 3D relationships and may be sensitive to slice selection and orientation. 3D approaches, while more holistic, face challenges related to the curse of dimensionality, increased model complexity, and overfitting due to smaller effective dataset sizes.¹⁴

The optimal choice between 2D and 3D approaches may depend on various factors, including the specific neurological condition being studied, the available dataset size, and the computational resources at hand. Moreover, the relative performance of different architectural paradigms (such as CNNs, ConvKANs, GCNs) may vary between 2D and 3D implementations, necessitating a comparative study.

This study evaluates new deep learning architectures for MRI analysis, evaluating and validating ConKANs for medical image classification and introducing the first 3D implementation of a ConvKAN. Novel interpretative visualisations for a ConvKAN are presented in both 2D and 3D dimensions, alongside visualisations for CNN and GCN architectures. By comparing these diverse approaches in both two and three

dimensions, the study aims to advance the understanding of optimal strategies for deep learning in neuroimaging.

Methods

This study utilised three open-source datasets: the Parkinson’s Progression Markers Initiative (PPMI) MRI dataset, NEUROCON and Tao Wu (Table 1).^{15,16} While all three datasets included both PD patients and age-matched healthy control subjects, there were differences in patient characteristics. The PPMI cohort was restricted to newly diagnosed PD patients within 2 years of diagnosis who had not yet started any PD medications. To ensure a fair comparison and robustly assess model performance across datasets, a subset of the PPMI dataset was randomly selected, matched for sample size and MRI sequence. The NEUROCON and Tao Wu datasets included PD patients with longer average disease durations, most of whom were already receiving treatment with dopaminergic medications such as levodopa.

Table 1: *Participant demographics in each dataset.*

	PPMI	NEUROCON	Tao Wu
Total Participants	59	43	40
Age (SD)	63·5 (11·1)	68·3 (11·0)	65·0 (5·0)
Number of PD	28	27	20
Number of Controls	31	16	20
Age PD (SD)	61·6 (10·4)	68·7 (11·0)	65·2(4·4)
Age Controls	64·2 (8·7)	67·6 (11·9)	64·8(5·6)
Disease Duration, years (SD)	1·7 (0·8)	4·8 (6·2)	5·4 (3·9)
Number of Males	26	21	23
Number of Females	33	22	17
MRI Sequence	MPRAGE (T1)	MPRAGE (T1)	MPRAGE (T1)

For the 2D analysis, 100 axial slices centered on the midbrain were extracted from each T1-weighted volume. The midbrain was chosen as the centre point due to its known involvement in PD pathology.¹⁷ For the 3D analysis, whole- brain volumes were resampled to 128 x 128 x 128 voxels using trilinear interpolation, preserving the full spatial information of the brain while standardizing the input dimensions for our 3D models. Figure 1 illustrates the MRI scans used in our analyses. Panel (a) depicts single slices centred on the midbrain, which were used individually in the 2D analyses. Panel (b) shows the entire volumetric MRI scan used for the 3D analyses.

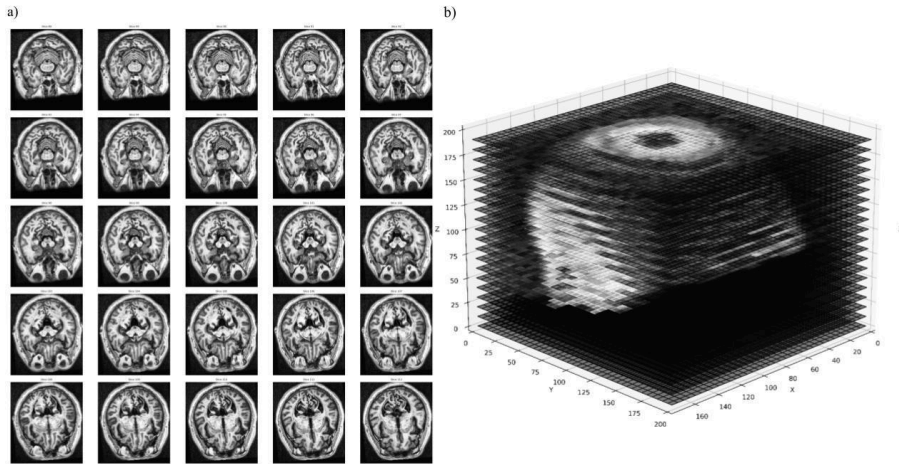


Figure 1: a) Example of single slices, centred on the midbrain, used individually to classify between PD and HC in the two-dimensional analyses. b) Entire volumetric MRI scan used in the three-dimensional analyses. Gaps are inserted at regular intervals to help visualise inner structure but are not implemented in the analyses.

The ConvKAN architecture, implemented in both 2D and 3D variants, extends the original ConvKAN principles to MRI analysis.⁹ Our models employ custom KANConv layers (KANConv2D for 2D and KANConv3D for 3D), which integrate traditional convolution operations with learnable B-spline functions for adaptive, non-linear transformations of input data (Supplementary Material 1). These spline functions are defined over a grid of 10 control points (knots), allowing them to flexibly adapt to complex patterns in the data. The original design is adapted by combining the spline outputs with a SiLU (Sigmoid Linear Unit) activation, creating a hybrid mechanism that balances adaptability with stable gradient properties.

Splines are flexible mathematical functions composed of smoothly connected polynomial segments. In the ConvKAN models, B-splines are used, which can accurately represent complex, smooth curves.¹⁸ As illustrated in Figure 2, this property is particularly valuable in medical image classification, where the distinction between healthy and diseased tissue often involves subtle intensity variations across the image, not fitting conventional convolutional filter shapes. Traditional CNNs typically use fixed convolutional filters, which apply the same spatial pattern matching to all input data. In contrast, our learnable splines can adapt their shape during training to better capture the unique intensity patterns and spatial relationships present in MRI scans. This adaptability allows the network to model the complex, often gradual transitions between different tissue types or structural changes indicative of pathology, theoretically improving diagnostic accuracy compared to methods using fixed, predetermined convolutional filters.

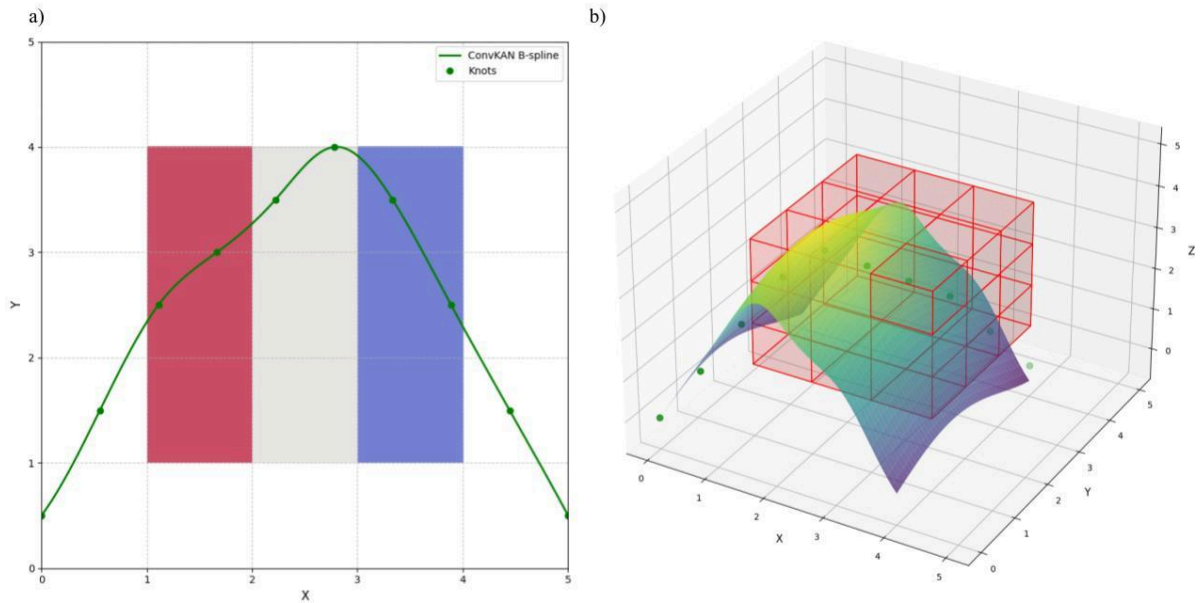


Figure 2: Comparison of ConvKAN splines and CNN convolutional filters in 2D and 3D dimensions. (a) 2D representation: The gridded square represents a single MRI slice. The coloured 3x3 region within the grid illustrates an example CNN filter, while the green curve demonstrates a B-spline used in ConvKAN, with green dots indicating knots. (b) 3D representation: The cube represents a volumetric MRI scan. The red 3x3x3 region within the cube shows a CNN filter, while the curved surface represents a 3D B-spline used in ConvKAN, with green dots marking the knots.

The 3D ConvKAN extension represents a novel application of KAN principles to volumetric medical imaging, enabling simultaneous capture of intricate spatial relationships in all dimensions. This approach is particularly relevant for neurological diagnosis, where the full three-dimensional structure of the brain may provide critical diagnostic information that might be missed in slice-by-slice analysis.

The GCN models transformed MRI data into graph representations (Supplementary Material 2). For the 2D analysis, MRI slices were transformed into graphs using the Simple Linear Iterative Clustering (SLIC) algorithm to generate 1000 superpixels per slice, each representing a node with features including mean intensity and relative area.¹⁹ Edges were established using a k-nearest neighbours approach (k=6) based on Euclidean distance between centroids.²⁰ For the 3D analysis, the SLIC algorithm was extended to create 1000 supervoxels per volume, with node features including mean intensity, relative volume, and normalised centroid coordinates, and edges also established using k-nearest neighbours (k=6). Figure 3 illustrates the graph creation process for GCN analysis. Panel (a) shows the 2D graph creation using superpixels, while panel (b) demonstrates the 3D graph representation using supervoxels. To validate the graph representations, several graph metrics were calculated, including average degree, clustering coefficient, and assortativity coefficient.

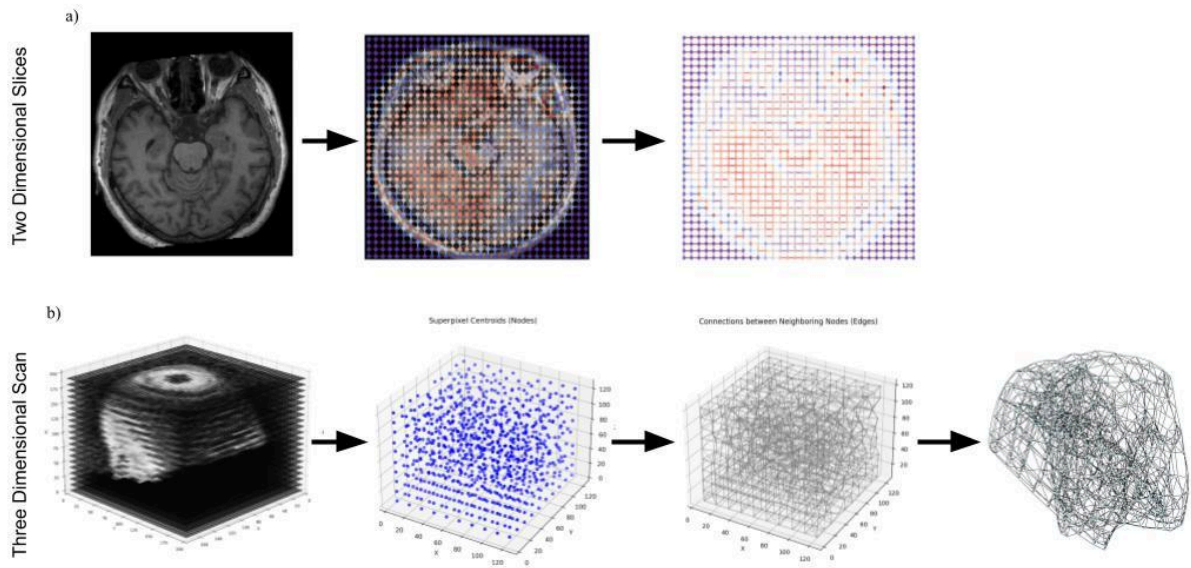


Figure 3: *Graph creation processes for GCN analysis. a) 2D graph creations, using superpixels, demonstrating alignment with anatomical features. (b) 3D graph representation of volumetric MRI, with nodes as supervoxels and edges as spatial relationships. Each node (sphere) represents a supervoxel, with node size indicating relative volume and colour representing mean intensity. Edges (lines) connect neighbouring supervoxels in 3D space.*

All models were trained using the Adam optimizer and early stopping with a patience of 15 epochs was employed to prevent overfitting. For 2D models, we used a five-fold stratified group cross-validation, ensuring the slices from a single subject were either all in the training set or all in the validation set, to stop any data leakage. For 3D models, due to the limited number of full brain scans, a Leave-One-Out Cross-Validation (LOOCV) strategy was employed. To address class imbalance, weighted cross-entropy loss was used, with weights inversely proportional to class frequencies in the training data.

To explore the interpretability of the models, preliminary visualisation techniques were developed for each architecture in both 2D and 3D (Supplementary Material 3). For CNNs and ConvKANs, activation maps of their respective layers were generated, with a focus on the spline layers in ConvKANs to illustrate their non-linear activations. For GCNs, t-Distributed Stochastic Neighbour Embedding (t-SNE) was used to project learned node embeddings into 3D space, visualising them alongside the original graph structure.²¹ For 3D models, these techniques were adapted to represent volumetric activations using 3D scatter plots. These visualisations were created for a subset of the test data, aiming to provide initial qualitative insights into the features processed by each model. However, it is important to note that these visualisations are exploratory, and their correlation with specific areas of pathology has not been established.

All models were trained using an NVIDIA A100 GPU via a publicly accessible cloud computing platform. Model performance was evaluated using accuracy, F1 score, and Area Under the Receiver Operating Characteristic Curve (AUROC).

Results

Varying performance across models and dimensionalities was observed. For 2D analysis, in the NEUROCON dataset, ConvKAN demonstrated the strongest performance with an AUROC of 0.83 and accuracy of 0.81, outperforming both CNN (AUROC 0.78, accuracy 0.76) and GCN (AUROC 0.55, accuracy 0.62). The 3D analysis of the same dataset revealed a shift in performance dynamics. While ConvKAN maintained the highest AUROC at 0.96, CNN showed superior accuracy at 0.91 compared to ConvKAN's 0.81. Notably,

GCN performance improved substantially in the 3D analysis, achieving an AUROC of 0.84, though still trailing behind both CNN and ConvKAN.

With the PPMI dataset there was strong performance across models, particularly in 3D analysis. In the 2D implementation, ConvKAN slightly bettered CNN with an AUROC of 0.98 and accuracy of 0.92, compared to CNN's AUROC of 0.96 and accuracy of 0.90. GCN performance in 2D was notably lower, with an AUROC of 0.59 and accuracy of 0.53. The 3D analysis of the PPMI dataset showcased the potential of these models, with ConvKAN achieving perfect classification (AUROC and accuracy of 1.00). Both CNN and GCN also demonstrated robust 3D performance, each attaining an AUROC of 0.97, though GCN showed higher accuracy (0.90) compared to CNN (0.80).

Results from the Tao Wu dataset presented a more mixed picture. In 2D analysis, while ConvKAN achieved the highest accuracy at 0.87, CNN marginally surpassed it in AUROC with 0.72 compared to ConvKAN's 0.71. GCN continued to show lower performance in 2D with an AUROC of 0.53 and accuracy of 0.43. The 3D analysis of the Tao Wu dataset saw CNN take the lead with a perfect AUROC of 1.00 and accuracy of 0.79. ConvKAN followed closely with an AUROC of 0.98 but demonstrated lower accuracy at 0.71. GCN performance, while improved in 3D, remained the lowest among the three models with an AUROC of 0.73 and accuracy of 0.57.

	Model	Accuracy	AUC-ROC	F1 Score
NEUROCON 2D	CNN	0.76	0.78	0.75
NEUROCON 2D	ConvKAN	0.81	0.83	0.81
NEUROCON 2D	GCN	0.62	0.55	0.48
NEUROCON 3D	CNN	0.91	0.95	0.91
NEUROCON 3D	ConvKAN	0.81	0.96	0.82
NEUROCON 3D	GCN	0.63	0.84	0.48
PPMI 2D	CNN	0.90	0.96	0.89
PPMI 2D	ConvKAN	0.92	0.98	0.92
PPMI 2D	GCN	0.53	0.59	0.36
PPMI 3D	CNN	0.80	0.97	0.79
PPMI 3D	ConvKAN	1.00	1.00	1.00
PPMI 3D	GCN	0.90	0.97	0.90
Tao Wu 2D	CNN	0.69	0.72	0.65
Tao Wu 2D	ConvKAN	0.87	0.71	0.81
Tao Wu 2D	GCN	0.43	0.53	0.27
Tao Wu 3D	CNN	0.79	1.00	0.77
Tao Wu 3D	ConvKAN	0.71	0.98	0.67
Tao Wu 3D	GCN	0.57	0.73	0.51

Table 2: *Classification metrics of models in both dimensional analyses*

Across all datasets, several consistent trends were observed (Figure 4). The impact of dimensionality was evident across all models and datasets, with 3D implementations typically yielding higher AUROC values compared to their 2D counterparts. ConvKAN demonstrated competitive or superior performance to CNNs, particularly in terms of AUROC. While GCN models generally showed lower performance compared to ConvKAN and CNN, they consistently improved in 3D analyses.

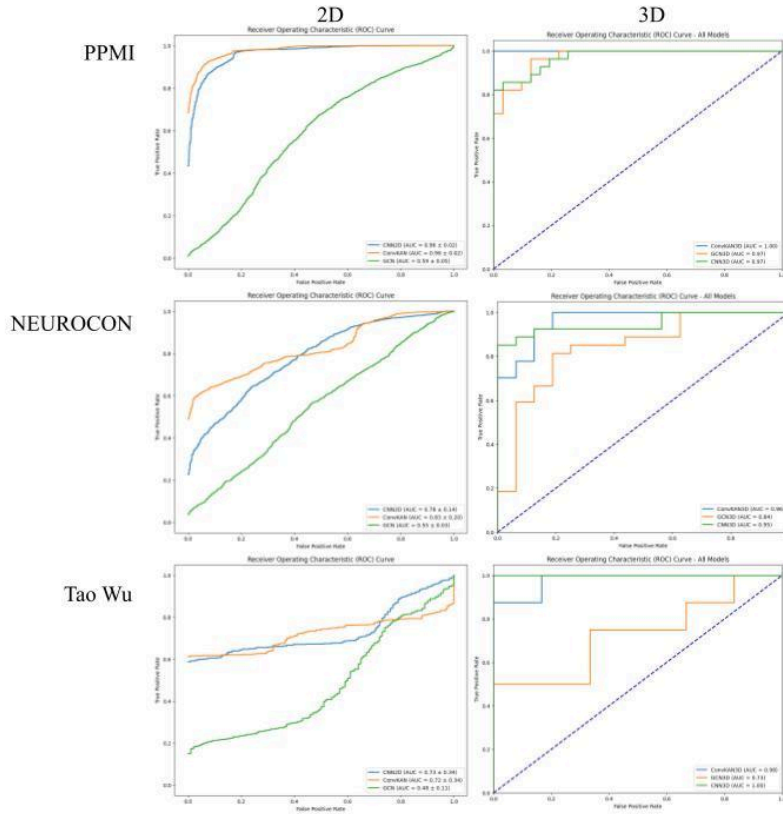


Figure 4: Mean AUROC (over all folds) of each model classifying two-dimensional slices individually, and the entire three-dimensional volumetric scan as a single data input. The increased granularity of the two dimension AUROC curves results from each individual slice being classified compared to the full scans classified after being used as a single data input in the three dimension analyses.

To validate the graph representations, a comparative analysis of graph properties between PD and control subjects was conducted for both 2D and 3D approaches. For 3D graphs, an average degree of 5.6, an average clustering coefficient of 0.21, and an average assortativity coefficient of 0.03 were observed, compared to 5.2, 0.18, and 0.02, respectively, for 2D graphs. The feature difference between PD and control graphs was larger in 3D (22.3) than in 2D (18.8), indicating that 3D graphs capture more distinctive attributes of PD pathology.

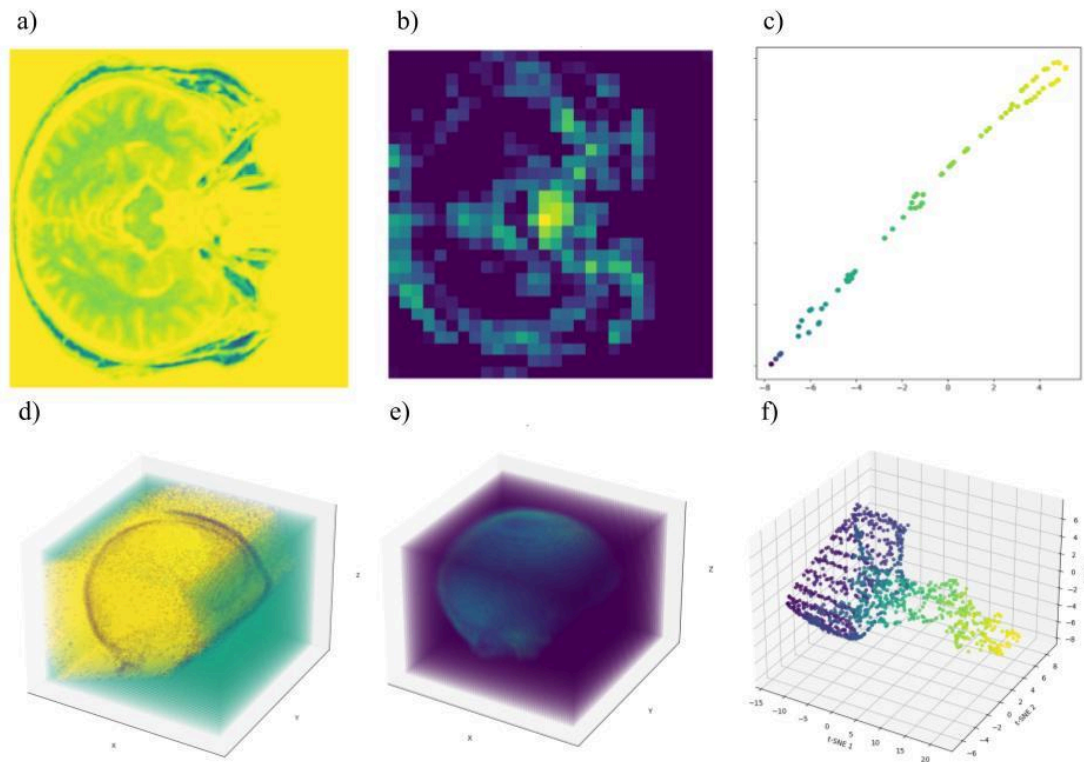


Figure 5: *Interpretability visualisations for ConvKAN, CNN, and GCN models in 2D and 3D. (a) 2D-ConvKAN activation map from the second SplineConv2d layer. (b) 2D-CNN activation map from the corresponding convolutional layer. (c) 2D-GCN t-SNE projection of node embeddings. (d) 3D-ConvKAN spline activation scatter plot from the second KANConv3D layer. (e) 3D-CNN activation scatter plot from the corresponding 3D convolutional layer. (f) 3D-GCN projection of node embeddings. All visualisations derived from the same representative slice or scan.*

To explore the features learned by the models, proof-of-concept visualisations were generated for a subset of the test data (Figure 5). The CNN and ConvKAN models produced activation maps in both 2D and 3D, with ConvKAN maps showing patterns of similar complexity to CNN. The GCN visualisations displayed clusters in the node embedding space for both 2D and 3D implementations. The 3D visualisations across all models revealed spatial relationships not apparent in 2D analyses.

Discussion

ConvKANs demonstrated promising performance across both 2D and 3D analyses, often matching or surpassing traditional CNNs. This high performance can be attributed to the architecture's unique combination of spatial invariance properties with flexible, non-linear modelling capabilities through learnable B-spline functions. In the context of PD neuroimaging, this adaptability is particularly relevant for capturing subtle, progressive structural changes that may elude traditional CNN architectures.

Notably, the 3D implementation of ConvKANs showed particular strength, achieving the highest AUROC (1.00) in the PPMI dataset, highlighting the potential of this approach in volumetric MRI analysis. The superior performance of all models on the PPMI dataset, particularly in the 3D implementations, might be partially attributed to the early stage characteristics of this cohort. This highlights the importance of considering disease stage when developing and evaluating AI-based diagnostic tools for PD, as this factor can significantly influence the detectability of disease-related brain changes. Importantly, structural MRI changes are not affected by

medication status, which is an advantage of this approach compared to physiological measures that may be confounded by treatment effects.

However, the performance of ConvKANs exhibited variability across datasets and dimensionalities, particularly in the Tao Wu dataset, underscoring the challenges in developing generalizable, dataset-agnostic foundation models for clinical neuroimaging. While ConvKANs excelled in certain scenarios, CNNs showed more consistent performance, especially in 3D implementations. This variability can be attributed to several factors, including differences in image acquisition parameters, patient demographics, and disease severity distribution across datasets.

From a clinical perspective, these findings highlight the importance of standardised imaging protocols and diverse patient cohorts in developing reliable AI-assisted diagnostic tools for PD. The variability in model performance across datasets emphasises the need for multi-cohort validation studies and careful consideration of dataset characteristics in the development and evaluation of AI models.

From a computational perspective, ConvKANs offer advantages over traditional CNNs that are particularly relevant in clinical settings. Their ability to achieve similar performance levels with fewer parameters, attributed to the use of learnable B-spline functions, can lead to faster training times and lower memory requirements. Such computational benefits could facilitate more efficient clinical workflows. The ability of ConvKANs to maintain high performance in both 2D and 3D implementations also offers flexibility in adapting to various clinical imaging protocols and legacy datasets.

The lower performance of Graph Convolutional Network (GCN) models, particularly in 2D analysis across all datasets, warrants further investigation. While graph-based approaches offer theoretical advantages in capturing global structural relationships, our results suggest that the conversion of 2D image data to graph representations may result in a loss of fine-grained spatial information crucial for detecting subtle PD-related changes. The improved performance of GCN in 3D analyses, especially in the PPMI dataset (AUROC 0.97), indicates that graph-based approaches may be more suitable for capturing global structural relationships in volumetric data or that medication is a large confounder. This finding matches a graph based study by Huang et al. and validates this 3D approach.¹¹

Our graph property analysis revealed notable differences between 2D and 3D representations, with 3D graphs consistently showing higher values across key metrics. These findings suggest that 3D graph representations capture a richer and more nuanced picture of brain structure compared to their 2D counterparts. The larger feature differences between PD and control graphs in 3D indicate that volumetric data encodes more distinctive attributes of PD pathology, explaining the superior performance of 3D GCN models.

Our interpretability analysis represents a preliminary step towards understanding model behaviour in both 2D and 3D contexts. The newly developed spline-activation maps for ConvKAN demonstrate the feasibility of visualising these adaptive, non-linear activations. However, like many deep learning interpretability methods, these visualisations face common challenges such as the difficulty in correlating activations with specific biological features, potential instability across different inputs, and the risk of confirming pre-existing biases rather than providing new insights.

Limitations should be noted. The sample sizes in the datasets were relatively small, limiting the generalisability of our findings. Future studies should aim to validate these results on larger, more diverse cohorts to ensure clinical applicability across different patient populations. The use of different cross-validation strategies for 2D and 3D analyses, while justified by the nature of the data (using entire 3D scans reduced training data so a 5-fold approach was not suitable), introduces bias in direct comparisons between dimensionalities. The focus on binary classification between PD patients and healthy controls, while a common approach, may oversimplify the complex spectrum of PD and fail to account for other neurodegenerative conditions such as atypical parkinsonian disorders. Moreover, the inherent "black box" nature of deep learning models, combined with this binary classification approach, raises the possibility that our models may be using non-PD related changes for classification. These could include global atrophy associated with normal ageing or overlapping conditions present in the patient cohort, rather than PD-specific markers. While our models demonstrate high performance, it's crucial to acknowledge this limitation in interpretability. Additionally, the retrospective nature of the datasets used means that we cannot account for variations in MRI acquisition parameters or clinical assessment protocols across different sites.

In conclusion, this study provides an evaluation of deep learning architectures for MRI-based PD classification, with the novel development and validation of ConvKANs to MRI data representing a significant contribution to the field. While MRI is not currently used as a primary diagnostic tool for PD, our findings suggest that with appropriate model selection and refinement, MRI analysis has the potential to become a valuable component of a multimodal diagnostic approach. Our findings highlight the importance of

a diverse model arsenal in deep learning-assisted diagnosis, with ConvKANs now added to this repertoire. As we move towards personalised medicine in neurodegenerative disorders, the integration of advanced imaging analysis with clinical expertise holds promise for improving patient outcomes through more precise diagnosis, prognosis, and treatment planning in PD.

Data Sharing

This study utilised three open-source datasets for model development and validation: the Parkinson's Progression Markers Initiative (PPMI) MRI dataset, the NEUROCON dataset, and the Tao Wu dataset. All datasets are publicly available and can be accessed through their respective online repositories: <https://www.ppmi-info.org/%20> and https://fcon_1000.projects.nitrc.org/indi/retro/parkinsons.html. The code used for model implementation and analysis will be made available on GitHub.

References

1. Morris HR, Spillantini MG, Sue CM, Williams-Gray CH. The pathogenesis of Parkinson's disease. *Lancet*. 2024;**403**(10423):293-304.
2. Ben-Shlomo Y, Darweesh S, Llibre-Guerra J, Marras C, San Luciano M, Tanner C. The epidemiology of Parkinson's disease. *Lancet*. 2024;**403**(10423):283-92.
3. Grover VP, Tognarelli JM, Crossey MM, Cox IJ, Taylor-Robinson SD, McPhail MJ. Magnetic Resonance Imaging: Principles and Techniques: Lessons for Clinicians. *J Clin Exp Hepatol*. 2015;**5**(3):246-55.
4. Marsili L, Rizzo G, Colosimo C. Diagnostic Criteria for Parkinson's Disease: From James Parkinson to the Concept of Prodromal Disease. *Front Neurol*. 2018;**9**:156.
5. Huang SC, Pareek A, Jensen M, et al. Self-supervised learning for medical image classification: a systematic review and implementation guidelines. *npj Digit Med*. 2023;**6**:74.
6. Liu X, Faes L, Kale AU, et al. A comparison of deep learning performance against health-care professionals in detecting diseases from medical imaging: a systematic review and meta-analysis. *Lancet Digit Health*. 2019;**1**(6):e271- 97.
7. Sarvamangala DR, Kulkarni RV. Convolutional neural networks in medical image understanding: a survey. *Evol Intell*. 2022;**15**(1):1-22.
8. [preprint] Liu Z, Wang Y, Vaidya S, et al. KAN: Kolmogorov-Arnold Networks. arXiv [cs.LG]. 2024. Available from: <https://arxiv.org/abs/2404.19756>
9. [preprint] Bodner AD, Tepsich AS, Spolski JN, Pourteau S. Convolutional Kolmogorov-Arnold Networks. arXiv [cs.CV]. 2024. Available from: <https://arxiv.org/abs/2406.13155>
10. [preprint] Drokin IS. Kolmogorov-Arnold Convolutions: Design Principles and Empirical Studies. arXiv [cs.LG]. 2024. Available from: <https://arxiv.org/html/2407.01092v1>
11. Huang L, Ye X, Yang M, Pan L, Zheng S. MNC-Net: Multi-task graph structure learning based on node clustering for early Parkinson's disease diagnosis. *Comput Biol Med*. 2023;**152**:106308.
12. El-Assy AM, Amer HM, Ibrahim HM, Farag AA. A novel CNN architecture for accurate early detection and classification of Alzheimer's disease using MRI data. *Nat Sci Rep*. 2024;**14**:3463.
13. Ravinder M, Saluja G, Allabun S, et al. Enhanced brain tumor classification using graph convolutional neural network architecture. *Nat Sci Rep*. 2023;**13**:14938.
14. Singh SP, Wang L, Gupta S, Goli H, Padmanabhan P, Gulyás B. 3D Deep Learning on Medical Images: A Review. *Sensors* . 2020;**20**(18):5097.
15. Marek K, Chowdhury S, Siderowf A, et al. The Parkinson's progression markers initiative (PPMI) - establishing a PD biomarker cohort. *Ann Clin Transl Neurol*. 2018;**5**(12):1460-1477.

16. Badea L, Onu M, Wu T, Roceanu A, Bajenaru O. Exploring the reproducibility of functional connectivity alterations in Parkinson's disease. *PLoS ONE*. 2017;**12**(11):e0188196.
17. Stern S, Lau S, Manole A, et al. Reduced synaptic activity and dysregulated extracellular matrix pathways in midbrain neurons from Parkinson's disease patients. *npj Parkinson's Disease*. 2022;**8**:103.
18. Kano H, Nakata H, Martin CF. Optimal curve fitting and smoothing using normalized uniform B-splines: a tool for studying complex systems. *Appl Math Comput*. 2005;**169**(1):96-128.
19. Achanta R, Shaji A, Smith K, Lucchi A, Fua P, Süsstrunk S. SLIC Superpixels Compared to State-of-the-art Superpixel Methods. *IEEE Trans Pattern Anal Mach Intell*. 2012;**34**(11):2274-82.
20. Chen M, Wang B, Li X. Deep Contrastive Graph Learning with Clustering-Oriented Guidance. *Proc AAAI Conf Artif Intell*. 2024;**38**(10):11364-72.
21. [preprint] Leow YY, Laurent T, Bresson X. GraphTSNE: A visualisation Technique for Graph-Structured Data. arXiv [cs.LG]. 2019. Available from: <https://arxiv.org/abs/1904.0691515>.

Supplementary Materials

1. Model Architectures and Rationale

We implemented three distinct neural network architectures - Convolutional Neural Networks (CNNs), Convolutional Kolmogorov-Arnold Networks (ConvKANs), and Graph Convolutional Networks (GCNs) - each in both 2D and 3D variations to process slice-based and volumetric MRI data, respectively.

Our 2D models process individual MRI slices of dimensions 224x224 pixels, extracted from the central region of the brain encompassing 100 axial slices. The 3D models operate on entire brain volumes resampled to 128x128x128 voxels. This dimensional choice balances spatial resolution with computational feasibility, allowing for feature extraction while managing memory constraints.

The 2D CNN comprises three convolutional layers with 32, 64, and 128 filters respectively, each using 3x3 kernels with stride 1 and padding 1. Each convolutional layer is followed by batch normalisation (momentum 0.1, epsilon 1e-5) and max pooling (2x2). The network concludes with an adaptive average pooling layer to produce a 1x1 spatial output, followed by two fully connected layers: the first with 128 units (dynamically adjusted based on the output of the convolutional layers) and the second with 2 units for binary classification.

The 3D CNN extends this architecture to volumetric data, employing four 3D convolutional layers with 32, 64, 128, and 256 filters, each using 3x3x3 kernels. Similar to its 2D counterpart, each convolutional layer is succeeded by batch normalisation and 3D max pooling (2x2x2). The network culminates in an adaptive 3D average pooling layer and two fully connected layers (128 units, then 2 units).

Both CNN variants utilise ReLU activation functions and incorporate dropout (p=0.5) before the final classification layer to mitigate overfitting.

As described in the original paper from June 2024, ConvKANs represent an innovative fusion of Kolmogorov-Arnold Network principles with convolutional architectures. The core innovation lies in the integration of learnable B-spline functions as adaptive, non-linear activations within the convolutional framework, offering enhanced flexibility in modeling complex relationships in MRI data.

2D ConvKAN Implementation:

Our 2D ConvKAN utilizes custom SplineConv2d layers. Each SplineConv2d layer consists of:

1. A standard 2D convolution operation.
2. A BSpline2D module with 10 learnable knots and associated weights.
3. A hybrid activation mechanism combining the B-spline output with a SiLU (Sigmoid Linear Unit) activation.

The forward pass of a SplineConv2d layer can be described as:

$$\text{output} = w1 * \text{spline}(\text{conv}(x)) + w2 * \text{silu}(\text{conv}(x))$$

where w_1 and w_2 are learnable parameters, $\text{spline}()$ is the B-spline function, and $\text{conv}()$ is the standard convolution operation.

The 2D ConvKAN architecture comprises:

- Three SplineConv2d layers with 32, 64, and 128 filters respectively (3x3 kernel, stride 1, padding 1)
- Each SplineConv2d layer is followed by batch normalization and max pooling (2x2)
- An adaptive average pooling layer
- Two fully connected layers (128 units, then 2 units for binary classification)

The 3D ConvKAN extends this concept to volumetric data using KANConv3D layers. Each KANConv3D layer includes:

1. A standard 3D convolution operation.
2. A BSpline3D module, again with 10 learnable knots, adapted for 3D inputs.
3. The same hybrid activation mechanism as in 2D, but applied to 3D data. The 3D ConvKAN structure consists of:
 - Four KANConv3D layers with 32, 64, 128, and 256 filters (3x3x3 kernel, stride 1, padding 1)
 - Each KANConv3D layer is followed by 3D max pooling (2x2x2)
 - A 3D adaptive average pooling layer
 - Two fully connected layers (256 to 64 units, then 2 units for classification)

In both 2D and 3D implementations, the B-spline functions allow for dynamic adaptation of the activation landscape during training. This adaptability enables the capture of more nuanced, non-linear features in the MRI data compared to traditional CNNs with fixed activation functions.

An important feature of our ConvKAN implementation is the adaptive grid extension mechanism, a concept introduced in the original ConvKAN paper. We extend this idea by implementing a dynamic process where the grid is automatically expanded by 25% when out-of-range inputs are encountered, with spline coefficients interpolated to maintain continuity. This approach ensures our B-spline functions can handle a wide spectrum of input values, enhancing the model's ability to capture complex, non-linear relationships in MRI data without being constrained by predetermined input bounds. Our implementation allows ConvKAN models to maintain flexibility and performance across varying intensity distributions in MRI scans.

The combination of convolutional operations, adaptive B-spline activations, and the hybrid mechanism with SiLU activation provides a flexible framework for capturing complex spatial relationships in both 2D slices and 3D volumes of MRI data, offering advantages in detecting subtle structural changes associated with Parkinson's Disease.

Our GCN models offer a fundamentally different approach to MRI analysis, representing the image data as graphs. This approach allows for the explicit modelling of structural relationships within the brain, which may be particularly relevant for detecting the subtle anatomical changes associated with PD.

For 2D analysis, each MRI slice is transformed into a graph with 1000 nodes, where each node represents superpixel. Node features include mean intensity and relative size of the superpixel. In the 3D case, we create a single graph per volume using 1000 supervoxels, with node features encompassing mean intensity, relative volume, and normalised centroid coordinates.

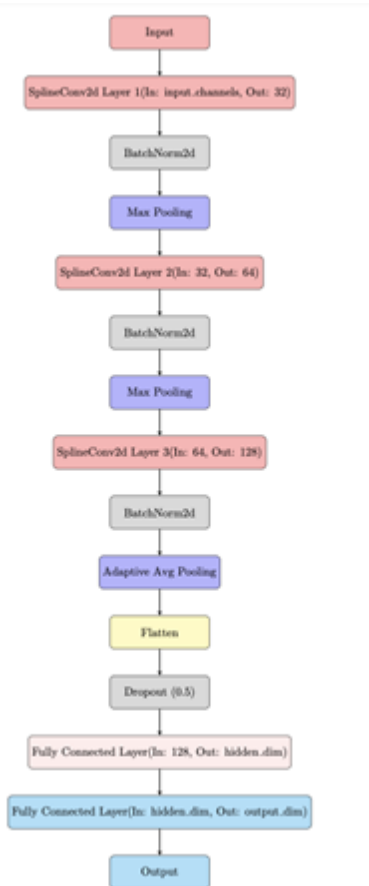
Edge connections in both 2D and 3D graphs are established using a k-nearest neighbours approach ($k=6$) based on the Euclidean distance between centroids. Edge weights are computed as the inverse of the distance between connected nodes.

The 2D GCN architecture comprises three GCNConv layers with 64 hidden channels each. The 3D GCN extends this to four GCNConv layers, maintaining 64 hidden channels. Both variants employ ReLU

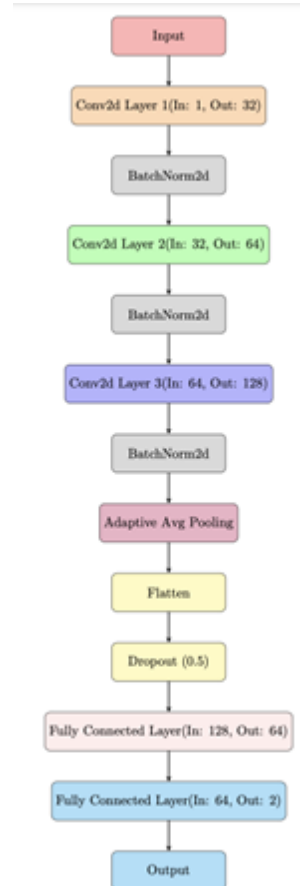
activation and dropout ($p=0.3$) after each GCNConv layer, followed by global mean pooling and a final linear layer for classification.

This graph-based approach allows our models to capture both local and global structural information in the MRI data, theoretically identifying patterns that might be overlooked by traditional convolutional approaches.

a)

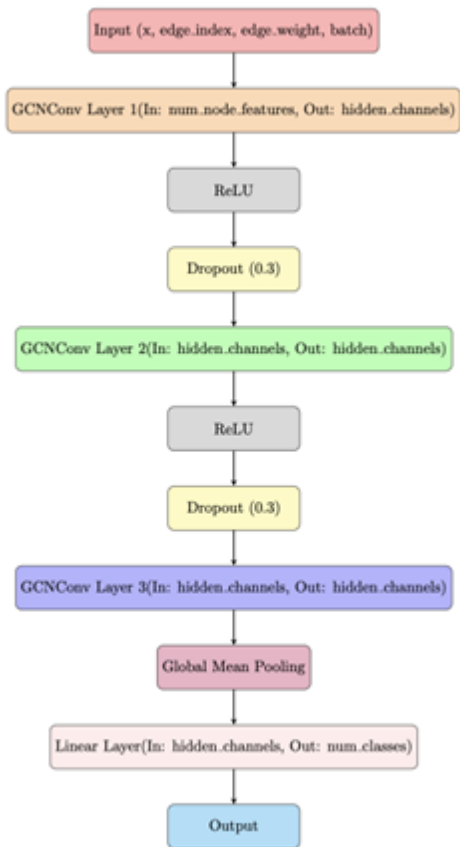


b)

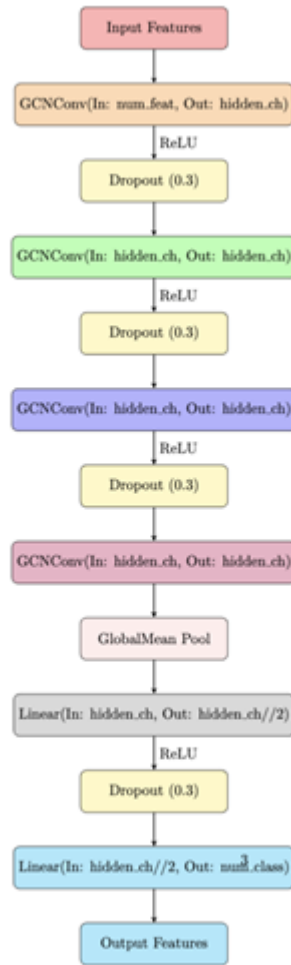


c)

d)



e)



f)

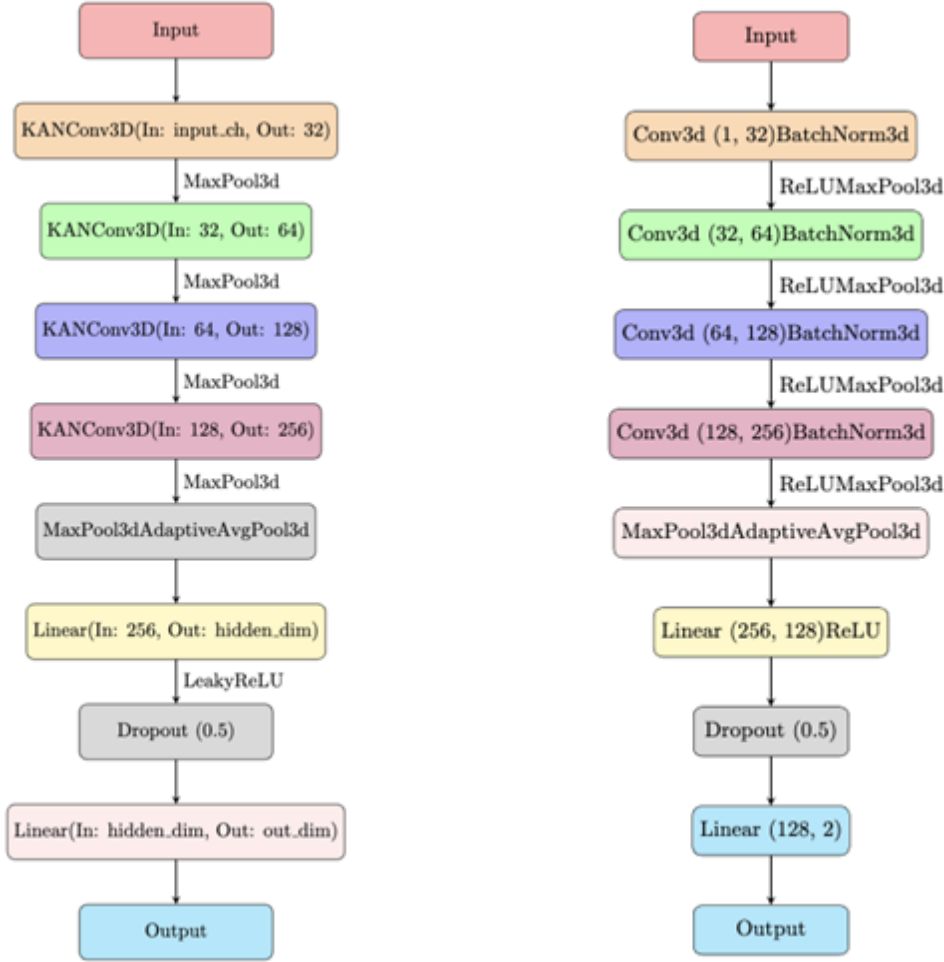


Figure S1: Architectural diagrams of the 2D and 3D implementations of ConvKAN, CNN, and GCN models.

Figure S1 illustrates the detailed structures of our six models for PD classification. (a) The 2D ConvKAN presents our 2D implementation, featuring SplineConv2d layers that merge traditional convolutions with learnable non-linear activations (b) The 2D CNN structure depicts our convolutional approach, highlighting the sequence of 2D convolutional layers, batch normalisation, and pooling operations. (c) The 2D GCN diagram illustrates how we process MRI slices as graphs, showing the sequence of GCNConv layers and global pooling. (d) The 3D GCN extends this graph-based approach to volumetric data, demonstrating how entire MRI volumes are analyzed as complex 3D graphs. (e) The 3D ConvKAN diagram showcases our novel volumetric implementation of the Convolutional Kolmogorov-Arnold Network, featuring KANConv3D layers that combine 3D convolutions with adaptive B-spline activations. (f) Finally, the 3D CNN diagram uses standard convolutional operations to process volumetric MRI data. Each diagram provides insights into the layer sequences, input/output dimensions, and key operations specific to each model type and dimensionality, facilitating a comprehensive comparison of our diverse architectural approaches to MRI analysis.

In all models, we employed the Adam optimizer with an initial learning rate of $1e-4$ and weight decay of $1e-5$. We implemented early stopping with a patience of 15 epochs, monitoring validation loss to prevent overfitting. For 2D models, we used a batch size of 64, while 3D models, due to memory constraints and the Leave-One-Out Cross-Validation strategy, used a batch size of 1.

2. Graph Creation

Our study employed graph-based approaches for both two-dimensional (2D) and three-dimensional (3D) MRI data analysis. This method is based upon the notion that structural relationships within brain imagery can be effectively captured and classified using graph representations. By transforming MRI data into graphs, we aimed to incorporate both local and global context, overcoming limitations of traditional convolutional approaches in capturing long-range dependencies and structural relationships.

For 2D analysis, we transformed each MRI slice into a graph representation using superpixel segmentation. Specifically, we employed the Simple Linear Iterative Clustering (SLIC) algorithm to generate 1000 superpixels per slice. SLIC was chosen for its ability to adhere to image boundaries while maintaining roughly equal-sized segments, which is crucial for creating meaningful graph representations of the MRI data.

Prior to segmentation, each slice was normalised to the range $[0, 1]$ to ensure consistent intensity scales across different MRI scans. The SLIC algorithm was then applied with a compactness parameter of 10, which balances the trade-off between spatial proximity and colour similarity. A small amount of Gaussian smoothing ($\sigma=1$) was applied to reduce noise and improve segmentation quality.

Each superpixel became a node in our graph. For each node, we extracted two key features:

1. Mean intensity: This feature represents the average pixel intensity within the superpixel, capturing the overall brightness or darkness of the region.
2. Relative area: Calculated as the area of the superpixel divided by the total area of the slice, this feature provides information about the size and the importance of each region.

These features were chosen to capture both intensity-based and structural information of the MRI slice, providing a balance between local intensity patterns and global structural characteristics.

Edge connections were established using a k-nearest neighbours approach with $k=6$, based on the Euclidean distance between superpixel centroids. This choice of $k=6$ was made to balance local connectivity with some degree of long-range interactions. Edge weights were computed as the inverse of $(1 + \text{distance})$ between connected nodes, encouraging the model to prioritise local connections while still allowing for some long-range interactions.

The use of k-nearest neighbours ensures that each node is connected to a consistent number of other nodes, preventing isolated subgraphs and ensuring information can flow throughout the entire graph structure. The inverse distance weighting scheme emphasises local connections while still allowing for the influence of more distant nodes, capturing both fine-grained local features and broader structural patterns in the MRI data.

For 3D analysis, we extended the concept of superpixels to volumetric data, using supervoxels instead. The SLIC algorithm was again employed to generate 1000 supervoxels per MRI volume. This choice of 1000 supervoxels balances the trade-off between capturing fine-grained structural information and maintaining computational efficiency.

Prior to segmentation, each 3D volume was resampled to a uniform size of $128 \times 128 \times 128$ voxels using trilinear interpolation. This resampling step ensures consistency across different MRI acquisitions and reduces computational complexity while preserving essential structural information.

For 3D graphs, we extracted three features for each node:

1. Mean intensity: The average voxel intensity within the supervoxel.
2. Relative volume: The volume of the supervoxel relative to the total brain volume.
3. Normalised centroid coordinates: The x , y , and z coordinates of the supervoxel centroid, normalised to the range $[0, 1]$.

These features were chosen to capture not only intensity and size information (as in the 2D case) but also spatial location within the brain volume. The inclusion of centroid coordinates allows the graph to retain information about the spatial arrangement of brain structures, which is crucial for capturing the 3D topology of the brain.

As in the 2D case, edge connections for 3D graphs were established using a k-nearest neighbours approach with $k=6$, based on the Euclidean distance between supervoxel centroids. The same inverse distance weighting scheme was applied to edge weights.

The use of superpixels/supervoxels instead of individual pixels/voxels offers several advantages:

1. Computational efficiency: By reducing the number of nodes in the graph, we significantly decrease computational complexity, allowing for faster training and inference.

2. Improved feature representation: Superpixels/supervoxels capture local structural information more effectively than individual pixels/voxels, as they represent coherent regions of the image.
3. Noise reduction: By aggregating features over regions rather than using individual pixel/voxel values, we reduce the impact of noise in the MRI data.

The choice of 1000 superpixels/supervoxels was made empirically to balance detail preservation with computational feasibility. This number allows for sufficiently fine-grained segmentation of brain structures while keeping the graph size manageable for subsequent processing steps.

To ensure our graph representations captured meaningful differences between Parkinson's Disease (PD) and control subjects, we calculated several graph metrics:

1. Average degree: Measures the average number of connections per node.
2. Average clustering coefficient: Quantifies the degree to which nodes tend to cluster together.
3. Average assortativity coefficient: Measures the preference for nodes to attach to similar nodes.

We also quantified the differences between PD and control graphs in terms of:

1. Feature difference: Calculated as the Euclidean distance between the mean node feature vectors of PD and control graphs.
2. Edge count difference: The absolute difference in the number of edges between PD and control graphs, normalised by the total edge count.
3. Node count difference: The absolute difference in the number of nodes between PD and control graphs, normalised by the total node count.

Our analysis revealed substantial distinctions in node attributes between PD and control graphs, with a feature difference of 22.3 for 3D graphs and 18.8 for 2D graphs. The edge count and node count differences suggested structural variations between PD and control brain networks. These metrics confirmed that our graph construction process captured discriminative information for the classification task in both 2D and 3D scenarios.

By carefully considering the balance between local and global information, computational efficiency, and noise reduction, we effectively captured the structural and intensity-based features of brain MRI scans. The validation metrics suggest that these graph representations successfully encode clinically relevant differences between PD and control subjects, providing a solid foundation for subsequent classification tasks.

3. Deep Learning Interpretability

Our study employed a range of interpretability techniques to visualise and understand the behaviour of our 2D and 3D neural network models for MRI-based Parkinson's Disease classification.

For 2D models, we implemented three distinct visualisation approaches. Our CNN visualisation technique involved forward-propagating an input MRI slice through the network and extracting activation maps from each convolutional layer post-ReLU activation. We visualised these activation maps using matplotlib, displaying the original input slice alongside four selected feature maps. This allowed for a qualitative assessment of the hierarchical feature learning process across different scales and abstraction levels within the network.

For the 2D ConvKAN model, we developed a custom visualisation approach to capture the unique properties of the SplineConv2d layers. We extracted and visualised the activation maps from each of the three SplineConv2d layers. This method captured the combined effect of the convolution operation and the subsequent spline transformation, offering insights into how ConvKAN's flexible, spline-based activations capture complex, non-linear relationships within the MRI data.

Our 2D GCN visualisation employed t-Distributed Stochastic Neighbor Embedding (t-SNE) to project the learned node embeddings into a 2D space. We visualised both the original graph structure and the t-SNE projection of node embeddings side by side, allowing us to observe how the GCN learns to embed the graph structure and node features into a lower-dimensional space.

For 3D models, we developed more sophisticated visualisation techniques to handle volumetric data. Our 3D CNN visualisation extended the 2D approach to three-dimensional activation maps. For each convolutional layer, we created 3D scatter plots where each voxel in the activation map was represented as a point in 3D space. The color and opacity of each point were determined by its activation value, normalized to the range

[0, 1]. This technique allowed us to observe how the 3D CNN identifies spatially coherent features across the entire brain volume.

Our 3D ConvKAN visualisation built upon the 3D CNN approach, with additional considerations for the unique properties of the KANConv3D layers. We created 3D scatter plots for the activation maps of each KANConv3D layer, similar to the CNN approach. Additionally, we implemented a separate visualisation specifically for the spline activation in the first KANConv3D layer, allowing us to observe how the learned B-spline functions transform the feature maps in three-dimensional space.

For the 3D GCN, while not implemented in the provided code, we proposed extending our t-SNE approach to create 3D embeddings of the learned node representations. This would allow visualisation of how the GCN learns to embed the 3D brain structure into a lower-dimensional space while preserving important topological relationships. Visualising these embeddings for each layer of the GCN would provide a view of how the representation evolves through the network.

Both 3D visualisation techniques for CNN and ConvKAN used matplotlib's 3D plotting capabilities. We created a 2x2 grid of 3D scatter plots for the CNN and ConvKAN layer activations, allowing for easy comparison of feature representations across different network depths. For the ConvKAN spline visualisation, we created a separate, larger 3D scatter plot to provide a detailed view of the spline transformation.

These visualisation techniques offer several advantages in understanding our models' behaviour. They provide a qualitative understanding of the features learned by each model, which is particularly valuable for identifying biologically relevant patterns in both 2D slices and 3D volumes. They allow for a comparative analysis between different architectural approaches (CNN, ConvKAN, and GCN) in both 2D and 3D contexts, highlighting the strengths and limitations of each. Furthermore, they serve as a tool for model debugging and refinement, revealing issues such as overfitting or failure to capture relevant features.

It is important to note that these visualisation techniques, while informative, are primarily proof-of-concept demonstrations for the ConvKAN architecture and its comparison with CNN and GCN models. The interpretability of these visualisations, particularly in 3D, can be challenging due to the complexity of the data and the limitations of representing 3D structures on a 2D display. Further quantitative analysis would be necessary to definitively prove the utility of these visualisations in a clinical context.